Strain and the optoelectronic properties of nonplanar phosphorene monolayers

Mehrshad Mehboudi[a], Kainen Utt[a], Humberto Terrones[b], Edmund O. Harriss[c], Alejandro A. Pacheco SanJuan[d], and Salvador Barraza-Lopez[a,1]

[a]Department of Physics, University of Arkansas, Fayetteville, AR 72701; [b]Department of Physics, Applied Physics, and Astronomy, Rensselaer Polytechnic Institute, Troy, NY 12180; [c]Department of Mathematical Sciences, University of Arkansas, Fayetteville, AR 72701; and [d]Departamento de Ingeniería Mecánica, Universidad del Norte, A. A. 1569 Barranquilla, Colombia

Edited by Monica Olvera de la Cruz, Northwestern University, Evanston, IL, and approved March 31, 2015 (received for review January 11, 2015)

Lattice kirigami, ultralight metamaterials, polydisperse aggregates, ceramic nanolattices, and 2D atomic materials share an inherent structural discreteness, and their material properties evolve with their shape. To exemplify the intimate relation among material properties and the local geometry, we explore the properties of phosphorene—a new 2D atomic material—in a conical structure, and document a decrease of the semiconducting gap that is directly linked to its nonplanar shape. This geometrical effect occurs regardless of phosphorene allotrope considered, and it provides a unique optical vehicle to single out local structural defects on this 2D material. We also classify other 2D atomic materials in terms of their crystalline unit cells, and propose means to obtain the local geometry directly from their diverse 2D structures while bypassing common descriptions of shape that are based from a parametric continuum.

phosphorene | discrete differential geometry | two-dimensional materials

Two-dimensional materials (1–20) are discrete surfaces that are embedded on a 3D space. Graphene (1, 2) develops an effective Dirac-like dispersion on the sublattice degree of freedom and other 2D atomic materials exhibit remarkable plasmonic, polariton, and spin behaviors too (18–20).

The properties of 2D materials are influenced by their local geometry (12–17, 21–29), making a discussion of the shape of 2D lattices a timely and fundamental endeavor (24, 30–32). A dedicated discussion of the shape of 2D materials is given here within the context of nets. Nets are discrete surfaces made from vertices and edges, with vertices given by particle/atomic positions (31–34). The discrete geometry that originates from these material nets is richer than its smooth counterpart because the net preserves the structural information of the 2D lattice completely, yielding exact descriptions of shape that remain accurate as the lattice is subject to arbitrarily large structural deformations (15, 16), as the particle/atomic lattice becomes the net itself.

A discrete geometry helps address how strain influences chemistry (35), how energy landscapes (36–38) correlate to nonplanar shapes, and it provides the basis for a lattice gauge theory for effective Dirac fermions on deformed graphene (39, 40). In continuing with this program, the optical and electronic properties of phosphorene cones will be linked to their geometry in the present work. At variance with 2D crystalline soft materials that acquire topological defects while conforming to nonplanar shapes (12–15), the materials considered here have strong chemical bonds that inhibit plastic deformations for strain larger than 10% (41).

The study is structured as follows: We build conical structures of black and blue phosphorene, determine their local shape, and link this shape to the magnitude of their semiconducting gap. It is clear that a discrete geometry applies for arbitrary 2D materials.

Results and Discussion

Phosphorene (8, 9) has many allotropes that are either semiconducting or metallic depending on their 2D atomistic structure (42–44). The most studied phase, black phosphorene (Fig. 1*A*), has a semiconducting gap that is tunable with the number of layers, and by in-plane strain (26, 27, 45, 46). Theoretical studies of defects on planar phosphorene indicate that dislocation lines do not induce localized electronic states (47), and algorithms to tile arbitrary planar 2D phosphorene patterns have been proposed as well (44). Unit cells of planar monolayers of black and blue phosphorene are displayed in Fig. 1.

Four invariants from the metric (g) and curvature (k) tensors determine the local geometry of a 2D manifold (24, 30):

$$\mathrm{Tr}(g),\ \mathrm{Det}(g),\ \ H \equiv \mathrm{Tr}(k)/2\mathrm{Tr}(g),\ \ K \equiv \mathrm{Det}(k)/2\mathrm{Det}(g), \qquad [1]$$

where Tr (Det) stands for trace (determinant), H is the mean curvature, and K is the Gaussian curvature.

An infinite crystal can be built from these unit cells, and the geometry of such ideal planar structure can be described by $\mathrm{Tr}(g)=1$, $\mathrm{Det}(g)=1$ (i.e., no strain), $H=0$, and $K=0$ (i.e., no curvature) at both sublayers S_1 and S_2. In addition, their thickness τ is equal to τ_0 before a structural distortion sets in: These five numbers quantify the local reference, flat geometry. [In principle, Tr(g) and Det(g) will be functions of the lattice constant, but here they are normalized with respect to their values in the reference crystalline structures seen in Fig. 1, to enable direct comparisons of the metric among black and blue phosphorene monolayers. $\tau_0=2.27$ (1.26) Å for black (blue) phosphorene in these planar reference structures.]

Now, structural defects can induce nonzero curvature and strain (35), and may also be the culprits for the chemical degradation of layered phosphorene. To study the consequences of shape on the optical and electronic properties of phosphorene monolayers, we create finite-size conical black and blue phosphorene monolayers, characterize the atomistic geometry, and investigate the influence of shape on their semiconducting gap. [We have proposed that hexagonal boron nitride could slow the degradation process while allowing for a local characterization of

Significance

Phosphorene is a new 2D atomic material, and we document a drastic reduction of its electronic gap when under a conical shape. Furthermore, geometry determines the properties of 2D materials, and we introduce discrete differential geometry to study them. This geometry arises from particle/atomic positions; it is not based on a parametric continuum, and it applies across broad disciplinary lines.

Author contributions: H.T., E.O.H., A.A.P.S., and S.B.-L. designed research; M.M., K.U., H.T., E.O.H., A.A.P.S., and S.B.-L. performed research; M.M., K.U., H.T., E.O.H., A.A.P.S., and S.B.-L. analyzed data; and S.B.-L. wrote the paper.

The authors declare no conflict of interest.

This article is a PNAS Direct Submission.

Freely available online through the PNAS open access option.

[1]To whom correspondence should be addressed. Email: sbarraza@uark.edu.

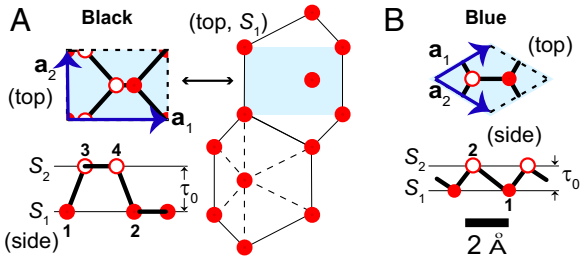

Fig. 1. Unit cells for (*A*) black and (*B*) blue phosphorene monolayers that are formed by two sublayers (S_1 and S_2) separated by a distance τ_0. Sublayers in black phosphorene are irregular—distances among nearest atoms belonging to the same sublayer are not identical—as emphasized by the dashed lines joining atoms belonging to sublayer S_1 on the rightmost structure in *A*.

phosphorene allotropes (48), and a study of chemical reactivity of nonplanar phosphorene will be presented elsewhere.]

Phosphorene cones are built from finite disk-like planar structures that have hydrogen-passivated edges (Fig. 2). The black phosphorene cone seen in Fig. 2*A* is created as follows: We remove an angular segment—that subtends a $\phi = 46°$ angle—from a planar structure that has a dislocation line (47). The two "ridges" that are highlighted by the red segments on the planar structure in Fig. 2*A* are joined afterward to create a disclination line. Atoms are placed in positions dictated by an initial (analytical) conical structure, and there is a full structural optimization via molecular dynamics at the ab initio level to relieve structural forces throughout (*Methods*).

Blue phosphorene has a (buckled) honeycomb structure reminiscent of graphene, so the conical structure seen to the left of Fig. 2*B* was generated by removing an angular segment subtending a $\phi = 60°$ angle on planar blue phosphorene, and following prescriptions similar to those used in creating the black phosphorene cone afterward.

The subplots displayed to the right in Fig. 2 *A* and *B* show the local discrete geometry at individual atoms (Eq. **1**; see details in *Methods*). For each allotrope, the data are arranged into three rows that indicate the geometry of the planar structure at sublayer S_1, and the local geometry of the cones at sublayers S_1 and S_2. An additional plot shows the value of τ/τ_0 that tells us of local vertical compression.

There is strain induced by the dislocation line on the planar black phosphorene structure, as indicated by the color variation on the Tr(g) and Det(g) plots, which implies having atoms at closer/longer distances than in the reference structure, Fig. 1. A slight curvature on the black phosphorene planar structure, induced by the dislocation line, is also visible in the H plot in Fig. 2*A*. The planar blue phosphorene sample does not have any dislocation line, and for that reason the metric shows zero strain [Tr(g) = 1 and Det(g) = 1] and zero curvature ($H = 0$ and $K = 0$) on that reference structure (Fig. 2*B*).

The black phosphorene conical structure seen in Fig. 2*A* has the following features: A compression near its apex, as displayed by the white color on the metric invariants; this compression is not radial-symmetric. An asymmetric elongation is visible toward the edges. In addition, there is a radially asymmetric nonzero curvature; the observed asymmetry reflects the presence of the

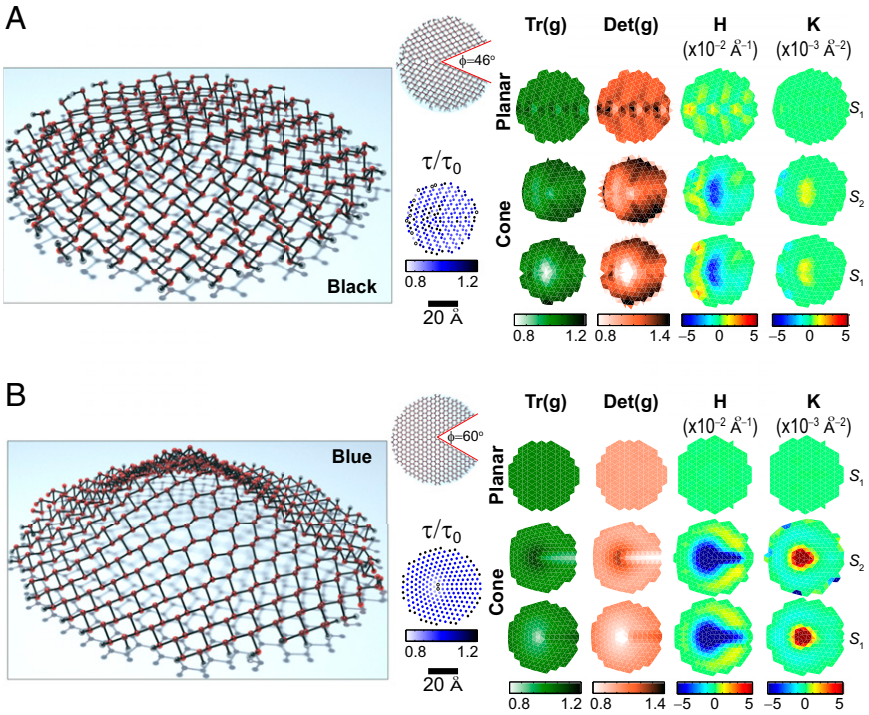

Fig. 2. (*A*) Black and (*B*) blue phosphorene cones are built by removing the angular segments in white from the planar structures (as illustrated at the upper-right corner of the conical structures), joining the cut structures along the red (disclination) lines, and a subsequent structural optimization. The discrete local geometry of these conical structures at sublayers S_1 and S_2 is given by four local invariants [Tr(g), Det(g), H, and K] that are obtained at each atomic position. These invariants are contrasted with the geometry of planar structures [Tr(g) = 1, Det(g) = 1, $H = 0$, and $K = 0$] that is depicted at the uppermost row for sublayer S_1. The change in relative height τ/τ_0 is shown at each atomic position as well. Features such as (*i*) strain induced by the dislocation line in planar black phosphorene, (*ii*) a sensible compressive strain near the apex, (*iii*) curvature lacking a radial symmetry, and (*iv*) the lack of significant changes in τ on conical black phosphorene, are clearly seen. The disclination line on the blue phosphorene cone is reflected on the metric invariants and on H: This disclination has a semicylindrical shape, which yields an overall radially symmetric Gaussian curvature K. In addition, a decrease of τ, and an in-plane compression (elongation) at sublayer S_1 (S_2) near the apex can also be seen on the blue phosphorene cone.

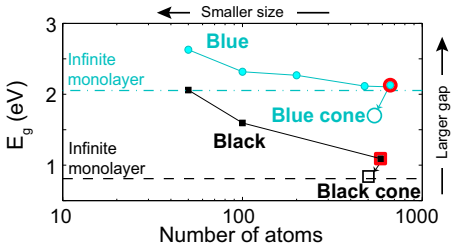

Fig. 3. The semiconducting gap of planar black and blue phosphorene monolayer disks increases as the number of atoms decreases. Even though the number of atoms must be reduced to create a conical shape from a planar structure, the gap decreases on conical structures with such decrease of the number of atoms, as indicated by open ticks and the tilted arrows: This reduction of the gap on a conical structure thus has a purely geometrical origin. (Dash and dash-dot lines indicate these gaps when the number of atoms is infinite.)

dislocation/disclination axis, which provides the structure with an enhanced structural rigidity. This rigidity is confirmed by the ratio τ/τ_0 close to unity, which indicates almost no vertical compression–elongation of this conical structure (Fig. 2*A*).

The blue phosphorene cone has a more apparent radial symmetry, except for the disclination line that is created by the conical structure, as reflected on the metric invariants and on H. There is compression (elongation) at the apex, and elongation (compression) along the disclination line in sublayer S_1 (S_2). The disclination line has a semicylindrical shape and hence a zero radius of curvature along the disclination line, resulting in a zero Gaussian curvature along such line; the Gaussian curvature looks radially symmetric overall.

Fig. 2 indicates that the blue phosphorene cone acquires the largest curvatures of these two cones. This is so because the angular segment removed from the planar blue phosphorene sample has a comparatively larger value of ϕ. One notes the rather smooth curvature at the apex on the blue phosphorene conical structure after the structural optimization.

The change of τ with respect to τ_0 is created by an out-of-plane strain or by shear. The blue phosphorene cone shows out-of-plane compression near the apex. The distance among planes in black phosphorene is closer to its value in an ideal planar structure throughout, showing scatter around the dislocation line.

The main point from Fig. 2 is the strain induced by curvature. The strain pattern observed in that figure is far more complex than those reported before for planar phosphorene (26, 27, 45, 46), and the discrete geometry captures the strain pattern with the precision given by actual atomic positions. We will describe the tools that lead to this geometry based from atoms later on (*Methods*), but we describe the effect of shape on the material properties of these cones first.

Black and blue phosphorene monolayers are both semiconducting 2D materials with a direct bandgap, and we investigate how this semiconducting gap evolves with their shape. The semiconducting gap $E_g =$ is equal to 1.1 (2.2) eV for the finite-size planar black (blue) phosphorene monolayers on display in Fig. 2, before the removal of the angular segments. These electronic gaps are highlighted at the rightmost end of Fig. 3. All gaps were computed after a structural optimization, to avoid unbalanced forces on these samples that would bias their magnitude (*Methods*).

We determine size effects on the semiconducting gap on planar structures first: The magnitude of the gap E_g increases as the number of atoms decreases on strain-free disk-like planar structures, as seen in Fig. 3. For an infinite number of atoms—i.e., for a fully periodic planar 2D crystal—the gap converges to the values indicated by the dash and dash-dot lines on Fig. 3, namely, 0.8 eV and 2.0 eV for black and blue phosphorene, respectively. These magnitudes were obtained from standard density-functional theory (8, 42). Although we acknowledge that other methods describe the dielectric properties more accurately on smaller samples (27), our focus is on the trend the gap follows, and given that the trend is geometrical in nature, it will stand correct despite the particular method used in computing the semiconducting gap.

The conical structures have fewer atoms than their parent planar structures once the angular segments seen in Fig. 2 *A* and *B* are removed. We learned in the previous paragraph that the electronic gap increases as the number of atoms is decreased on planar structures. Following that argument, one may expect the semiconducting gap for the conical structures to be larger than the one observed on their parent planar structures.

However, instead of increasing with the removal of atoms, the gap decreases dramatically on the conical structures, going down to 0.84 (1.70) eV for the black (blue) phosphorene cone, as indicated by the open red symbols, and the tilted arrows in Fig. 3: Shape influences phosphorene's material properties. A practical consequence of this result is that optical probes could provide a measure of the local shape of phosphorene. The relation between the semiconducting gap and a nonplanar shape has been observed in transition metal dichalcogenide monolayers recently (25), and we establish here that structural defects on semiconducting 2D materials create a similar effect. Let us next address the reason for such reduction of the semiconducting gap.

The semiconducting gap is a global material property. On finite samples it is possible to project the electronic density onto individual atoms to learn about the spatial localization of the

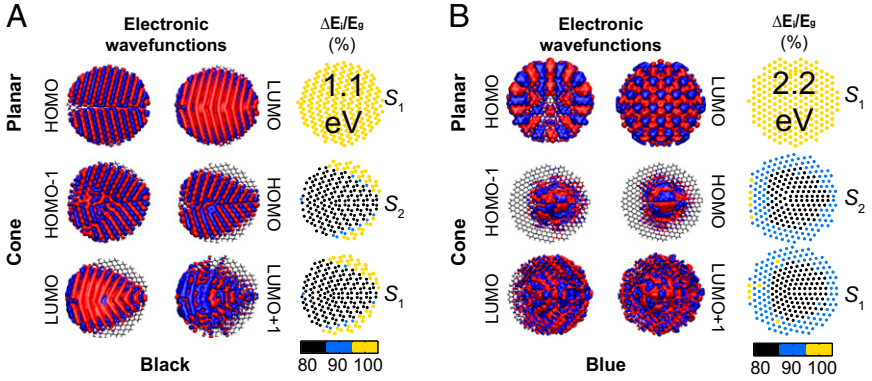

Fig. 4. A remarkable reduction of the semiconducting gap occurs due to the strain induced by the conical shape, and regardless of phosphorene allotrope. The local distribution of ΔE_i correlates with the extent of the electronic wavefunctions shown below and above the Fermi level for (*A*) black and (*B*) blue phosphorene.

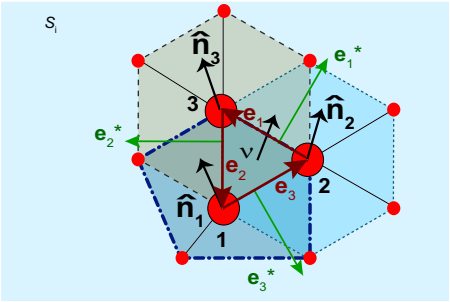

Fig. 5. Discrete tensors based on triangulations are expressed in terms of averaged normals $\hat{\mathbf{n}}_j$, edges $\mathbf{e}_j$, the normal of the triangle ν, and dual edges $\mathbf{e}_j^* \equiv \mathbf{e}_j \times \nu$ ($j = 1,2,3$). These tensors can be used in quad-nets, irregular lattices, and structures containing defects as highlighted by the pentagon surrounding atom **1**.

electronic states below and above the Fermi level, whose energy difference is equal to the electronic gap. Those states are known as the highest occupied molecular orbital (HOMO) and the lowest unoccupied molecular orbital (LUMO), and they were spin-degenerate in all of the samples we studied. Additionally, the nth electronic orbital below (above) the HOMO (LUMO) is labeled HOMO–n (LUMO+n).

The HOMO and LUMO states cover the entire planar black and blue phosphorene structures (Fig. 4) and are thus delocalized. On the other hand, the conical samples have orbitals below and above the Fermi energy that display a certain amount of localization.

Such effect is most visible for the HOMO and HOMO–1 states for the blue phosphorene cone in Fig. 4*B*. Thus, unlike a dislocation line (47) the pentagon defect that is responsible for the curvature of the blue conical structure is localizing the HOMO state within an ∼10 Å radius. Given that the pentagon defect originates curvature itself, we conclude that curvature leads to a reduction of the electronic gap on this system.

Given the localization observed on some of these orbitals, we can further ask: At a given atomic position, what is the first orbital with a nonzero density at such location below and above the Fermi energy? This question can be rephrased in terms of the difference in energy among the first orbitals below and above the Fermi level that have a nonzero probability density at a given atomic location: In the third column in Fig. 4 *A* and *B* we display such energy difference ΔE_i at every phosphorus atom i. There exists a clear correlation among ΔE_i and the localization pattern of the orbitals below and above the Fermi energy, as should be the case. The reduction on the semiconducting gap on the cones is emphasized by normalizing ΔE_i in terms of E_g, which yields a 20% reduction of the semiconducting gap for both allotropes: a nonplanar geometry that is created by structural defects on any phosphorene allotrope will lead to a sizable reduction of the semiconducting gap.

To end this work, we must state that the discrete geometry used to tell the shape of the phosphorene conical structures applies to other 2D atomic materials with varied unit cells, some of which are listed here: (*i*) Regular honeycomb lattices [graphene (2, 39, 40, 49) and hexagonal boron nitride (4)]. (*ii*) Low-buckled honeycomb hexagonal lattices [silicene and germanene (5); we established that freestanding stanene (50) is not the structural ground state]. (*iii*) "High-buckled" hexagonal close-packed bilayers of bismuth (51), tin, and lead (52). (*iv*) Thin trigonal–prismatic transition-metal dichalcogenides (53, 54). (*v*) Materials with buckled square unit cells—quad-graphs (31)—such as AlP (7).

Structures (*i*)–(*iv*) are equilateral triangular lattices with a basis, for which individual planes represent regular equilateral triangular nets; and structure (*v*) realizes a regular quad-graph.

Low-buckled structures (silicene, germanene, blue phosphorus), hexagonal close-packed bilayers (bismuth, tin, and lead), and black phosphorus have two parallel sublayers, S_1 and S_2. Transition-metal dichalcogenides and AlP have three parallel sublayers S_1–S_3. The discrete geometry clearly stands for other 2D materials that do not form strong directional bonds (12, 14) as well.

Concluding Remarks

Shape is a fundamental handle to tune the properties of 2D materials, and the discrete geometry provides the most accurate description of 2D material nets. This geometry was showcased on nonplanar phosphorene allotropes for which the electronic gap decreases by 20% with respect to its value on planar structures. The discrete geometry can thus be used to correlate large structural deformations to intended functionalities on 2D materials with arbitrary shapes.

Methods

Creation of Conical Structures. Consider structures having atomic positions at planar disks; these positions can be parameterized by r_i, θ_i, and $z_i = \{0, \tau_0\}$. Calling ϕ the angular segments being removed from these planar structures, the range of the angular variable θ_i is $[0,2\pi - \phi]$, and the conical structures are initially built by the following transformation: $r_i' = r_i\sqrt{1-(\phi^2/4\pi^2)}$, $\theta_i' = (2\pi/(2\pi-\phi))\theta_i$, and $z_i' = z_i - r_i(\phi/2\pi)$. These conical structures containing about 500 atoms undergo a structural optimization via ab initio (Car–Parinello) molecular dynamics (55) with the SIESTA code (56, 57), until forces are smaller than 0.04 eV/Å.

Calculation of the Electronic Gap of Phosphorene Samples. We obtain ΔE_i as follows: Let E_F be the charge neutrality level or Fermi energy, and $\rho_i(E)$ the density of electronic states projected onto atom i. We call E_i^A (E_i^B) the first energy level observed on $\rho_i(E)$ lying above (below) E_F at atom i, and report $\Delta E_i/E_g \equiv (E_i^A - E_i^B)/E_g$ in Fig. 4. We note that all structures we worked with had a final net zero spin polarization on spin-polarized calculations.

A Discrete Geometry Based on Triangulations at Atomic Positions. There is an extrinsic and continuum (Euclidean) geometry in which material objects exist. These material objects are made out of atoms that take specific locations to generate their own intrinsic shape.

The intrinsic shape of 2D atomic materials can be idealized as a continuum: The basic assumption of continuum mechanics is that a continuum shape is justified at length scales l much larger than interatomic distances that are characterized by a lattice parameter a_0 ($l \gg a_0$). The common understanding of shape arises from within this continuum perspective that is based on the differential geometry of 2D manifolds. This continuum approximation is valid down to interatomic scales ($l \leq a_0$) for slowly varying deformations, but not when curvature concentrates at atomic-scale bonds or pleats, such as in the examples provided in refs. 11 and 14. And so, whereas these sharp structures may be disregarded or approximated within the context of a continuum surface, we hold the opinion that an intrinsic geometry that is exact at the atomic scale must form part of the theoretical toolset to deal with 2D materials. The discrete geometry to be described in the next paragraphs bypasses descriptions of shape that are based on an effective continuum, and it brings an understanding of the shape of material nets at a fundamental level.

Consider three directed edges $\mathbf{e}_1$, $\mathbf{e}_2$, and $\mathbf{e}_3$, such that $\mathbf{e}_1 + \mathbf{e}_2 + \mathbf{e}_3 = \mathbf{0}$, and define $Q_l^l \equiv \mathbf{e}_l \cdot \mathbf{e}_l$ ($l = 1,2,3$), representing the square of the smallest finite distance among atoms on the 2D lattice. This is the discrete analog of the infinitesimal length element ds^2 (Fig. 5).

Now consider the change in orientation among normals $\hat{\mathbf{n}}_j$ and $\hat{\mathbf{n}}_k$, and project such variation onto their common edge $\mathbf{e}_l$: This is, define $Q_l^{ll} \equiv (\hat{\mathbf{n}}_k - \hat{\mathbf{n}}_j) \cdot \mathbf{e}_l$ (see Fig. 5; j, k, l are permutations of integers 1, 2, and 3). The reader may recall that the curvature tensor is defined as $\hat{n} \cdot (\partial g_\alpha / \partial \xi_\beta)$, but the discrete tensor carries a constant edge, and it rests on changes of the local normals instead. In the previous equation, $\hat{\mathbf{n}}_l$ is the average over individual normals at triangulated area elements within the polygon surrounding atom l and highlighted by dashed lines. The dual edge is defined by $\mathbf{e}_l^* \equiv \mathbf{e}_l \times \nu$, with ν the normal to the triangle formed by atoms **1**, **2**, and **3** and A_T is the triangle area ($-\mathbf{e}_2 \times \mathbf{e}_1 = 2A_T\nu$).

This way, the discrete metric tensor takes the following form on the basis given by dual edges*:

*Weischedel C, Tuganov A, Hermansson T, Linn J, Wardetzky M (2012) Construction of discrete shell models by geometric finite differences, The 2nd Joint Conference on Multibody System Dynamics, May 29–June 1, 2012, Stuttgart, Germany.

$$g = -\frac{1}{8A_0^2} \sum_{(j,k,l)} \left(Q_j^I - Q_k^I - Q_l^I \right) \mathbf{e}_j^* \otimes \mathbf{e}_j^*, \quad [2]$$

with A_0 the area of the triangulated area element at the reference (nondeformed and defect-free) plane.

The discrete curvature tensor has an identical structure:

$$k = -\frac{1}{8A_T^2} \sum_{(j,k,l)} \left(Q_j^{II} - Q_k^{II} - Q_l^{II} \right) \mathbf{e}_j^* \otimes \mathbf{e}_j^*. \quad [3]$$

The parentheses (j, k, l) indicate a sum of three terms, as follows: ($j = 1$, $k = 2$, $l = 3$), (2, 3, 1), and (3, 1, 2). Eqs. **2** and **3** become 3×3 matrices with explicit values for Q_j^I, Q_j^{II}, and $\mathbf{e}_j^*$ from atomic positions (Fig. 5). For instance, the discrete curvature tensor has eigenvalues {0, k_1, k_2} at each triangulated area element, yielding $H = (k_1 + k_2)/2$ and $K = k_1 k_2$. The geometrical invariants reported at point **j** are averages over their values at individual triangles sharing this vertex.

Topological defects (exemplified by a pentagon seen by a dot-dash line in Fig. 5) break translation symmetry, making it impossible to recover a crystalline structure by means of elastic deformations. However, Eqs. **2** and **3** provide a geometry along topological defects seamlessly still, as seen in the geometry provided in Fig. 2.

The computation of the distribution of the thickness τ in both conical structures was performed by finding for each atom in the lower sublayer S_1 the three nearest neighbors on the upper sublayer S_2. The distance between the centroid of these three atoms and the atom in question at the S_1 sublayer amounts to the thickness τ of the structure at that specific atom.

ACKNOWLEDGMENTS. This work was supported by the Arkansas Biosciences Institute (S.B.-L.) and by NSF EFRI-1433311 (to H.T.). Calculations were performed at Arkansas' Razor II and Texas Advanced Computing Center's Stampede (NSF-XSEDE, TG-PHY090002).

1. Novoselov KS, et al. (2005) Two-dimensional gas of massless Dirac fermions in graphene. *Nature* 438(7065):197–200.
2. Katsnelson MI (2012) *Graphene: Carbon in Two Dimensions* (Cambridge Univ Press, Cambridge, UK), 1st Ed.
3. Novoselov KS, et al. (2005) Two-dimensional atomic crystals. *Proc Natl Acad Sci USA* 102(30):10451–10453.
4. Jin C, Lin F, Suenaga K, Iijima S (2009) Fabrication of a freestanding boron nitride single layer and its defect assignments. *Phys Rev Lett* 102(19):195505.
5. Cahangirov S, Topsakal M, Aktürk E, Sahin H, Ciraci S (2009) Two- and one-dimensional honeycomb structures of silicon and germanium. *Phys Rev Lett* 102(23): 236804.
6. Zhang Y, et al. (2010) Crossover of the three-dimensional topological insulator Bi_2Se_3 to the two-dimensional limit. *Nat Phys* 6(8):584–588.
7. Zhuang HL, Singh AK, Hennig RG (2013) Computational discovery of single-layer III-V materials. *Phys Rev B* 87:165415.
8. Liu H, et al. (2014) Phosphorene: An unexplored 2D semiconductor with a high hole mobility. *ACS Nano* 8(4):4033–4041.
9. Li L, et al. (2014) Black phosphorus field-effect transistors. *Nat Nanotechnol* 9(5): 372–377.
10. Kane CL, Mele EJ (2005) Quantum spin Hall effect in graphene. *Phys Rev Lett* 95(22): 226801.
11. Castle T, et al. (2014) Making the cut: Lattice kirigami rules. *Phys Rev Lett* 113(24): 245502.
12. Bausch AR, et al. (2003) Grain boundary scars and spherical crystallography. *Science* 299(5613):1716–1718.
13. Vitelli V, Lucks JB, Nelson DR (2006) Crystallography on curved surfaces. *Proc Natl Acad Sci USA* 103(33):12323–12328.
14. Irvine WTM, Vitelli V, Chaikin PM (2010) Pleats in crystals on curved surfaces. *Nature* 468(7326):947–951.
15. Irvine WTM, Hollingsworth AD, Grier DG, Chaikin PM (2013) Dislocation reactions, grain boundaries, and irreversibility in two-dimensional lattices using topological tweezers. *Proc Natl Acad Sci USA* 110(39):15544–15548.
16. Gomes KK, Mar W, Ko W, Guinea F, Manoharan HC (2012) Designer Dirac fermions and topological phases in molecular graphene. *Nature* 483(7389):306–310.
17. Grason GM, Davidovitch B (2013) Universal collapse of stress and wrinkle-to-scar transition in spherically confined crystalline sheets. *Proc Natl Acad Sci USA* 110(32): 12893–12898.
18. Gutiérrez HR, et al. (2013) Extraordinary room-temperature photoluminescence in triangular WS2 monolayers. *Nano Lett* 13(8):3447–3454.
19. Dai S, et al. (2014) Tunable phonon polaritons in atomically thin van der Waals crystals of boron nitride. *Science* 343(6175):1125–1129.
20. Zibouche N, Philipsen P, Kuc A, Heine T (2014) Transition-metal dichalcogenide bilayers: Switching materials for spintronic and valleytronic applications. *Phys Rev B* 90: 125440.
21. Funkhouser CM, et al. (2013) Mechanical model of blebbing in nuclear lamin meshworks. *Proc Natl Acad Sci USA* 110(9):3248–3253.
22. Vernizzi G, Sknepnek R, Olvera de la Cruz M (2011) Platonic and Archimedean geometries in multicomponent elastic membranes. *Proc Natl Acad Sci USA* 108(11): 4292–4296.
23. Yao Z, Olvera de la Cruz M (2014) Polydispersity-driven topological defects as order-restoring excitations. *Proc Natl Acad Sci USA* 111(14):5094–5099.
24. Vozmediano MAH, Katsnelson MI, Guinea F (2010) Gauge fields in graphene. *Phys Rep* 496(4-5):109–150.
25. Castellanos-Gomez A, et al. (2013) Local strain engineering in atomically thin MoS_2. *Nano Lett* 13(11):5361–5366.
26. Rodin AS, Carvalho A, Castro Neto AH (2014) Strain-induced gap modification in black phosphorus. *Phys Rev Lett* 112(17):176801.
27. Fei R, Yang L (2014) Strain-engineering the anisotropic electrical conductance of few-layer black phosphorus. *Nano Lett* 14(5):2884–2889.
28. van der Zande A, Hone J (2012) Inspired by strain. *Nat Photonics* 6(12):804–806.
29. Meza LR, Das S, Greer JR (2014) Strong, lightweight, and recoverable three-dimensional ceramic nanolattices. *Science* 345(6202):1322–1326.
30. Kamien RD (2002) The geometry of soft materials: A primer. *Rev Mod Phys* 74(4): 953–971.
31. Bobenko AI, Suris YB (2008) *Discrete Differential Geometry. Integrable Structure, Graduate Studies in Mathematics* (American Mathematical Society, Providence, RI), 1st Ed, Vol 98.
32. Bobenko AI, Schröder P, Sullivan JM, Ziegler GM (2008) *Discrete Differential Geometry, Oberwolfach Seminars* (Birkhäuser, Basel, Switzerland), 1st Ed, pp 175–188.
33. Grinspun E, Wardetzky M, Desbrun M, Schröder P, eds (2008) *Discrete Differential Geometry: An Applied Introduction.* Available at ddg.cs.columbia.edu. Accessed November 2, 2014.
34. Xu Z, Xu G (2009) Discrete schemes for Gaussian curvature and their convergence. *Comput Math Appl* 57(7):1187–1195.
35. Haddon RC (1993) Chemistry of the fullerenes: The manifestation of strain in a class of continuous aromatic molecules. *Science* 261(5128):1545–1550.
36. Wales DJ (2004) *Energy Landscapes: Applications to Clusters, Biomolecules and Glasses* (Cambdridge Univ Press, Cambridge, UK), 1st Ed.
37. Wales DJ, Salamon P (2014) Observation time scale, free-energy landscapes, and molecular symmetry. *Proc Natl Acad Sci USA* 111(2):617–622.
38. Kusumaatmaja H, Wales DJ (2013) Defect motifs for constant mean curvature surfaces. *Phys Rev Lett* 110(16):165502.
39. Pacheco-Sanjuan AA, Wang Z, Pour-Imani H, Vanević M, Barraza-Lopez S (2014) Graphene's morphology and electronic properties from discrete differential geometry. *Phys Rev B* 89:121403.
40. Pacheco Sanjuan AA, Mehboudi M, Harriss EO, Terrones H, Barraza-Lopez S (2014) Quantitative chemistry and the discrete geometry of conformal atom-thin crystals. *ACS Nano* 8(2):1136–1146.
41. Lee G-H, et al. (2013) High-strength chemical-vapor-deposited graphene and grain boundaries. *Science* 340(6136):1073–1076.
42. Zhu Z, Tománek D (2014) Semiconducting layered blue phosphorus: A computational study. *Phys Rev Lett* 112(17):176802.
43. Guan J, Zhu Z, Tománek D (2014) Phase coexistence and metal-insulator transition in few-layer phosphorene: A computational study. *Phys Rev Lett* 113(4):046804.
44. Guan J, Zhu Z, Tománek D (2014) Tiling phosphorene. *ACS Nano* 8(12):12763–12768.
45. Rudenko AN, Katsnelson MI (2014) Quasiparticle band structure and tight-binding model for single- and bilayer black phosphorus. *Phys Rev B* 89:201408.
46. Cakir D, Sahin H, Peeters FM (2014) Tuning of the electronic and optical properties of single-layer black phosphorus by strain. *Phys Rev B* 90:205421.
47. Liu Y, Xu F, Zhang Z, Penev ES, Yakobson BI (2014) Two-dimensional mono-elemental semiconductor with electronically inactive defects: The case of phosphorus. *Nano Lett* 14(12):6782–6786.
48. Rivero P, et al. (2015) Simulated scanning tunneling microscopy images of few-layer phosphorus capped by graphene and hexagonal boron nitride monolayers. *Phys Rev B* 91:115413.
49. Guan J, et al. (2014) Local curvature and stability of two-dimensional systems. *Phys Rev B* 90:245403.
50. Xu Y, et al. (2013) Large-gap quantum spin Hall insulators in tin films. *Phys Rev Lett* 111(13):136804.
51. Sabater C, et al. (2013) Topologically protected quantum transport in locally exfoliated bismuth at room temperature. *Phys Rev Lett* 110(17):176802.
52. Rivero P, Yan J-A, García-Suárez VM, Ferrer J, Barraza-Lopez S (2014) Stability and properties of high-buckled two-dimensional tin and lead. *Phys Rev B* 90:241408.
53. Wang QH, Kalantar-Zadeh K, Kis A, Coleman JN, Strano MS (2012) Electronics and optoelectronics of two-dimensional transition metal dichalcogenides. *Nat Nanotechnol* 7(11):699–712.
54. Chhowalla M, et al. (2013) The chemistry of two-dimensional layered transition metal dichalcogenide nanosheets. *Nat Chem* 5(4):263–275.
55. Car R, Parrinello M (1985) Unified approach for molecular dynamics and density-functional theory. *Phys Rev Lett* 55(22):2471–2474.
56. Soler J, et al. (2002) The SIESTA method for ab-initio order-N materials simulation. *J Phys Condens Matter* 14(11):2745–2779.
57. Perdew JP, Burke K, Ernzerhof M (1996) Generalized gradient approximation made simple. *Phys Rev Lett* 77(18):3865–3868.